The Astrophysical Journal, 1000:277 (14pp), 2026 April 1 https://doi.org/10.3847/1538-4357/ae4903

Few Made It Out: A Multimessenger Study of an In Situ Solar Energetic Electron Event Driven by a Solar Jet

Meiqi Wang[1], Bin Chen[1], Mallory Wickline[1], Sijie Yu[1], Säm Krucker[2,3], Jeongwoo Lee[1], and Haimin Wang[1]
[1] Center for Solar-Terrestrial Research, New Jersey Institute of Technology, 323 Martin Luther King Boulevard, Newark, NJ 07102-1982, USA
[2] University of Applied Sciences and Arts Northwestern Switzerland (FHNW), Bahnhofstrasse 6, 5210 Windisch, Switzerland
[3] Space Sciences Laboratory, University of California, 7 Gauss Way, Berkeley, CA 94720, USA
Received 2025 October 2; revised 2026 February 17; accepted 2026 February 19; published 2026 March 27

Abstract

When in situ solar energetic electron (SEE) events are closely associated with nonthermal flares, the escaping electron population is frequently observed to be much smaller than the nonthermal-radiation-emitting population near the solar surface. If a single accelerated population drives both signatures, the physical mechanism causing this severe deficit of upward-propagating electrons remains poorly understood. Focusing on one of the 2022 November 10–12 SEE events associated with recurrent solar jets and interplanetary type III radio bursts, we present a new, combined microwave–X-ray analysis using the Expanded Owens Valley Solar Array and the Spectrometer/Telescope for Imaging X-rays on board Solar Orbiter. For the first time for such an event, this synergy enables spatially resolved diagnostics over a broad energy spectrum of the near-Sun energetic electrons, complemented by in situ measurements made by spacecraft at multiple heliocentric longitudes and distances. Consistent with earlier results based on in situ and X-ray data, our results show that only 0.1%–1% of energetic electrons escape into interplanetary space. Crucially, the new microwave spectral imaging analysis suggests that energetic electrons are strongly concentrated in a compact region just above a miniflare arcade at the base of the jet spire and that their number density decreases by at least 2 orders of magnitude in the direction of the jet spire away from this region. This steep gradient, revealed by the microwave diagnostics, points to efficient local acceleration and trapping in the region analogous to the above-the-loop-top "magnetic bottle" region in major eruptive flares, allowing only a small fraction of electrons to access open magnetic field lines and enter interplanetary space.

Unified Astronomy Thesaurus concepts: Solar energetic particles (1491); Solar radio emission (1522); Solar flares (1496); Solar x-ray emission (1536)

1. Introduction

Solar energetic electron (SEE) events involve the release of energetic electrons associated with solar activity, with energies ranging from a few keV to ∼MeV (D. V. Reames 1999). A group of SEE events features a relatively short duration and is sometimes referred to as "impulsive" or "prompt" SEE events. They are closely associated with magnetic reconnection processes occurring on the Sun and typically accompanied by ^{3}He enrichment (R. P. Lin et al. 1996; D. V. Reames 2021). They have been reported to be closely associated with type III radio bursts, which are driven by energetic electrons traveling along open magnetic field lines (L. Wang et al. 2012), and solar jets (N. V. Nitta et al. 2006, 2008; Y. M. Wang et al. 2006; S. Krucker et al. 2011; R. Bučík 2020). As both type III radio bursts and jets involve open field lines, it has been interpreted that energetic electrons can access and escape into interplanetary space through interchange magnetic reconnection with the ambient magnetic field lines (K. Shibata et al. 1992, 1996). However, studies suggest that some impulsive SEE events are associated with coronal mass ejections (CMEs), extreme-ultraviolet (EUV) waves, or other complex processes (M. E. Wiedenbeck et al. 2013; N. V. Nitta et al. 2015, 2023; R. Bučík et al. 2015).

Joint remote sensing observations and in situ measurements provide a more comprehensive picture of the acceleration and transport of energetic electrons from near the solar surface to interplanetary space. However, it remains an outstanding question whether the SEEs observed in interplanetary space share the same origin as those emitting nonthermal microwave or hard X-ray (HXR) emissions near the solar surface. Multiple studies comparing the spectra of HXR-emitting energetic electrons near the surface with those from in situ measurements have identified a positive correlation between their spectral indices, suggesting that they likely share a common origin (S. Krucker et al. 2007; N. Dresing et al. 2021; W. Wang et al. 2021). However, it is puzzling that these studies comparing the number of HXR-emitting and in situ measured energetic electrons found that only a very small fraction of electrons, ∼0.1%–1%, escape into interplanetary space, compared to the HXR-emitting population near the surface (S. Krucker et al. 2007; N. Dresing et al. 2021; W. Wang et al. 2021; M. Wang et al. 2025). This observed highly imbalanced partition significantly deviates from the scenario sometimes presumed, where particle acceleration occurs at a common site in the corona and ejects an equal number of energetic electrons in both upward and downward directions (see, e.g., the standard flare scenario depicted in K. Shibata et al. 1995).

One possible explanation is that initial acceleration occurs in the relatively high corona (W. Wang et al. 2021). Under this model, upward-propagating electrons escape directly into interplanetary space, while the downward-propagating

electrons undergo an additional acceleration process in the newly closed field near the surface, leading to an increased number of X-ray-emitting electrons (S. Krucker et al. 2007; W. Wang et al. 2021). One of the main arguments favoring this multiple-acceleration-site scenario is that some of the observed SEEs have power-law spectra extending down to several keV, which is deemed inconsistent with pure injection from the low solar corona, since the low-energy electrons would have experienced significant Coulomb collisional loss (W. Wang et al. 2021). Recent statistical studies (W. Wang et al. 2023, 2024) also argued that, despite a positive correlation, electron spectra derived from the thick-target HXR model are inconsistent with those of the in situ electrons, which also appears to argue against the common acceleration site scenario.

The other scenario, recently suggested by B. Chen et al. (2024), is that the accelerated electrons are strongly trapped in a nearly closed "magnetic bottle" region located below the reconnection X point, with only a small fraction managing to escape upward. This scenario naturally explains the highly imbalanced partition between the number of HXR/microwave-emitting electrons near the solar surface and the escaped in situ electrons, as well as their positive correlation with each other. However, more detailed investigations are needed to account for other observed phenomena.

On the other hand, the estimation of the total number of escaping electrons can be significantly affected by energy-dependent transport effects (R. P. Lin 1985; E. P. Kontar & H. A. S. Reid 2009; R. D. Strauss et al. 2020). The electrons can experience Coulomb collisions during their propagation from the corona to interplanetary space, with the lower-energy electrons enduring more significant losses (R. P. Lin 1985). Furthermore, E. P. Kontar & H. A. S. Reid (2009) propose that beam-driven plasma turbulence and solar wind density inhomogeneities play a critical role in producing the spectral break often observed in the electron spectra, resulting in flattening at lower energies (typically tens of keV). In addition to the various transport effects that influence low-energy electrons, R. D. Strauss et al. (2020) suggest that the energy loss of higher-energy electrons due to pitch-angle scattering contributes to spectral softening in the higher energy range. Thus, multiple spacecraft at various longitudinal and radial positions can provide valuable insight into the transport of energetic electrons in interplanetary space. They can also improve the estimation of the angular spread of the energetic electrons into interplanetary space and offer refinements of the estimations of the number of escaping electrons (see, e.g., H. Xie et al. 2019).

As for the remote sensing diagnostics of the energetic electrons near the solar surface, HXR bremsstrahlung emission provides excellent diagnostics of energetic electrons from $\sim$10 to 100 keV (J. C. Brown 1971). However, due to the sensitivity limitation of current X-ray instrumentation, it remains challenging to routinely observe the X-ray spectra above $\sim$100 keV except for large events. In addition to bremsstrahlung radiation, nonthermal electrons gyrating in the coronal magnetic field can emit gyrosynchrotron radiation in the microwave range. Although microwave emission is contributed by a broad spectrum of energetic electrons, the peak contribution usually comes from the electron population at $\gtrsim$100 keV (S. Krucker et al. 2020). Thanks to their sensitivity to different energy regimes, joint analysis of both X-ray and microwave data is particularly powerful for constraining energetic electron distribution over a wide energy regime (S. M. White et al. 2011; B. Chen et al. 2021). Since 2017, the Expanded Owens Valley Solar Array (EOVSA; D. E. Gary et al. 2018) has provided microwave imaging spectroscopy spanning from 1 to 18 GHz with a 1 s time resolution, enabling spatially resolved spectral analysis near the acceleration site. The availability of microwave imaging spectroscopy, together with complementary X-ray observations, allows us to constrain the energetic electron population over a wide energy range, improving the comparisons to the in situ measurements.

In this work, we investigate a series of SEE events associated with EUV solar jets observed by Solar Orbiter (SolO; D. Müller et al. 2020) in 2022 mid-November, a period of good magnetic connectivity between the spacecraft and the jets' source active region. These SEEs have been reported by D. Lario et al. (2024), who conducted a detailed investigation into their relationship with EUV jets, type III radio bursts, HXR flares, and associated CMEs. They suggested that most of the SEE events exhibit a strong temporal and spatial association with HXR flares and EUV jets. Here, we extend the investigation of these SEE events by focusing on a subset of events associated with a solar active region that is magnetically connected to the SolO spacecraft. We then carry out a detailed case study on a specific SEE event associated with a blowout solar jet. By integrating HXR and microwave imaging spectroscopy from the Spectrometer/Telescope for Imaging X-rays (STIX; S. Krucker et al. 2020) on board SolO and EOVSA, respectively, with multispacecraft in situ measurements from various heliocentric longitudes and distances, we develop a more comprehensive understanding of SEE acceleration and transport.

The plan of this paper is as follows. Section 2 provides a brief overview of these SEEs in association with type III radio bursts and solar jets. Section 3 presents a focused study of the event that occurred on 2022 November 12. After first providing a brief introduction to the event and its context, we conduct a detailed analysis utilizing multiwavelength remote sensing data and in situ measurements. Finally, in Section 4, we summarize our main findings and discuss their implications, with a special focus on understanding why only a small fraction of energetic electrons can escape to interplanetary space.

2. The Context: A Series of SEE Events

During the period from 2022 November 9 to 2022 November 14, the Energetic Particle Detector (EPD; J. Rodríguez-Pacheco et al. 2020) on board SolO observed a series of SEE events. Figure 1(a) shows the locations of multiple spacecraft, including SolO, STEREO-A, and Parker Solar Probe (PSP), on 2022 November 12 (produced using the Solar Mach Python package; J. Gieseler et al. 2023). SolO was positioned at a distance of 0.61 au from the Sun, while PSP was located at 0.67 au.

A total of 32 SEE events during this period were detected by SolO as previously reported by D. Lario et al. (2024), who investigated the relationships among SEEs, solar jets, type III radio bursts, and STIX flares. A detailed summary of the events is provided in Table 1 of D. Lario et al. (2024). In addition to SolO/EPD, this series of SEE events was also recorded by the Wind 3D Plasma and Energetic Particle instrument (3DP; R. P. Lin et al. 1995) on board

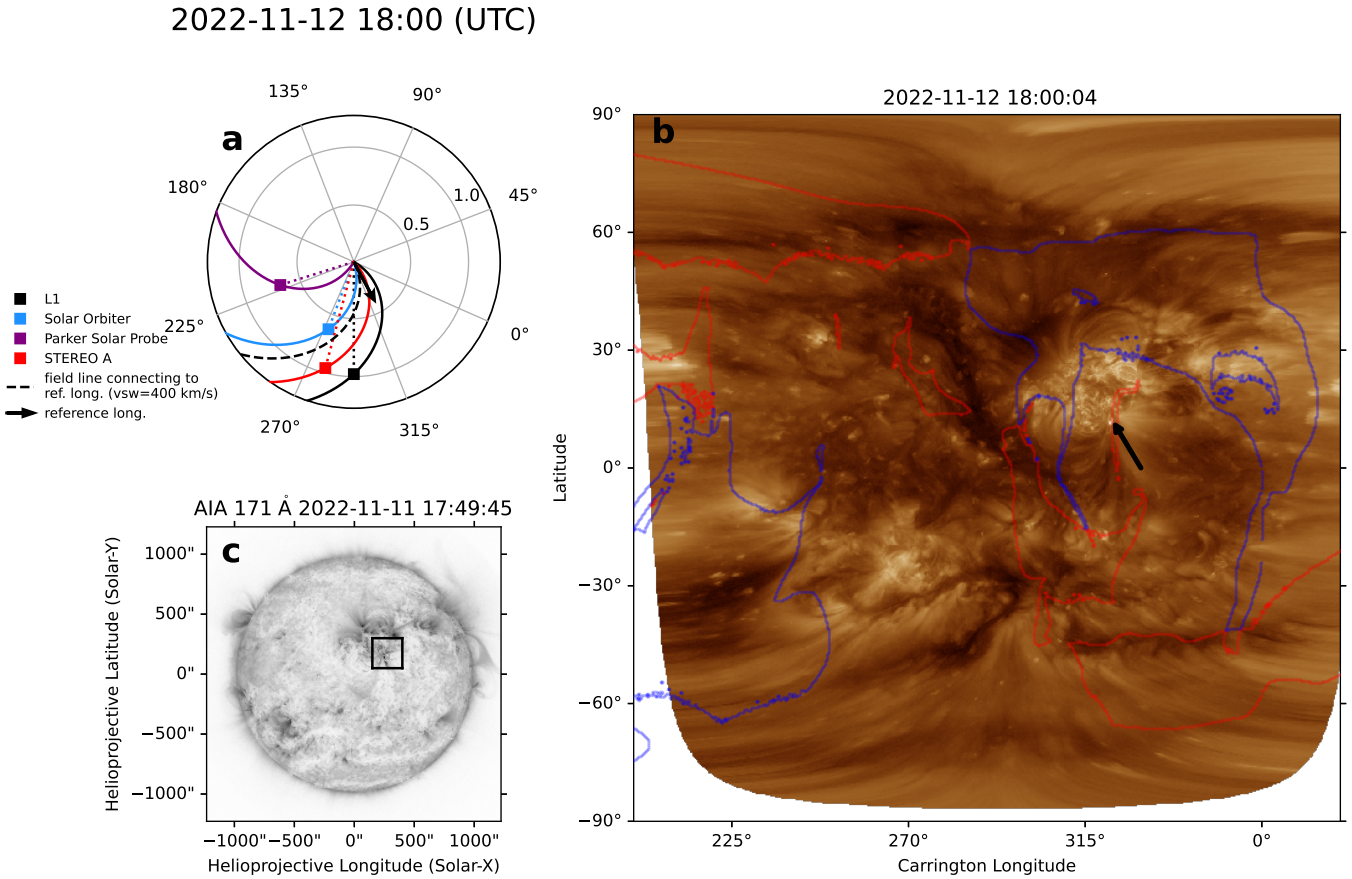

Figure 1. (a) Spacecraft configuration on 2022 November 12. The black arrow represents the longitude of AR 13141. The solar wind speed is assumed to be 400 km s^{-2}. (b) Open–closed field map of CR 2264 derived from the 3D MAS model. The background is the SDO/AIA 193 Å map reprojected into the Carrington coordinates. The red and blue contours mark the regions of open magnetic fields of positive and negative polarity, respectively. The black arrow indicates the jet region, which is associated with positive open magnetic field lines at the western edge of AR 13141. (c) Full-disk image from the SDO/AIA 171 Å channel at 17:49:45 UT on 2022 November 11. The black rectangle encloses AR 13141.

WIND and the Solar Electron and Proton Telescope (SEPT; R. Müller-Mellin et al. 2008) on board STEREO-A. Figures 2(a)–(c) display the electron flux in three selected energy channels as observed by SolO/EPD, STEREO-A/SEPT, and WIND/3DP, respectively. As described in Appendix B of D. Lario et al. (2024), the Sun aperture on board STEREO-A/SEPT was not pointed toward the Sun during the event period. To facilitate a more accurate comparison of electron flux among different spacecraft, we employ sector-averaged flux for SolO/EPD and STEREO-A/SEPT, calculated as the mean of the electron flux measured by detectors oriented in different viewing directions. For WIND, we use the omnidirectional electron flux data that are already available. In the STEREO-A electron flux profiles shown in Figure 2(b), multiple spikes are observed, each of which corresponds to an SEE event detected by SolO.

Out of the 32 SEE events, 25 are temporally associated with AR 13141 (Figure 1(b)). This active region has been reported to be prolific in producing recurrent jets in its periphery region, possibly due to sunspot rotation (T. Gou et al. 2024). It also has a small longitudinal separation from the nominal footpoint of SolO (following the ballistic Parker spiral) during the period from 2022 November 10 to 12 (Figure 3), suggesting a good magnetic connectivity to the SolO spacecraft. Recognizing the good magnetic connectivity to AR 13141, our study extends the work of D. Lario et al. (2024) by further focusing on these 25 SEEs and investigating their detailed spatial and temporal association with the recurrent jets, aiming to identify their specific physical origin. These events are also included in the CoSEE-Cat, an extensive catalog of SEEs observed by SolO (A. Warmuth et al. 2025).

To further investigate the magnetic field properties surrounding the recurrent jet region, we adopt a three-dimensional (3D) coronal model (magnetohydrodynamic algorithm outside a sphere model; Z. Mikić et al. 1999), which is derived using radial synoptic magnetograms computed from 720 s line-of-sight magnetograms obtained by the Helioseismic and Magnetic Imager (HMI; P. H. Scherrer et al. 2012) on board the Solar Dynamics Observatory (SDO) during Carrington rotation 2264. The 3D model is then used to trace magnetic field lines from 1 to 30 $R_\odot$ from a dense grid of heliographic latitudes and longitudes, which are, in turn, used to evaluate areas with open or closed field lines. The resulting "open–closed" field map[4] is shown in Figure 1(b), with red and blue contours enclosing open field regions with positive and negative polarity, respectively. We find that the recurrent jet region is located in the close vicinity of a narrow open field region, suggesting that SEEs associated with these jets may have access to the magnetic field opening to interplanetary space.

[4] The open–closed map is synonymous with the "coronal hole map" terminology used on the Predictive Science website: https://www.predsci.com/mhdweb/home.php.

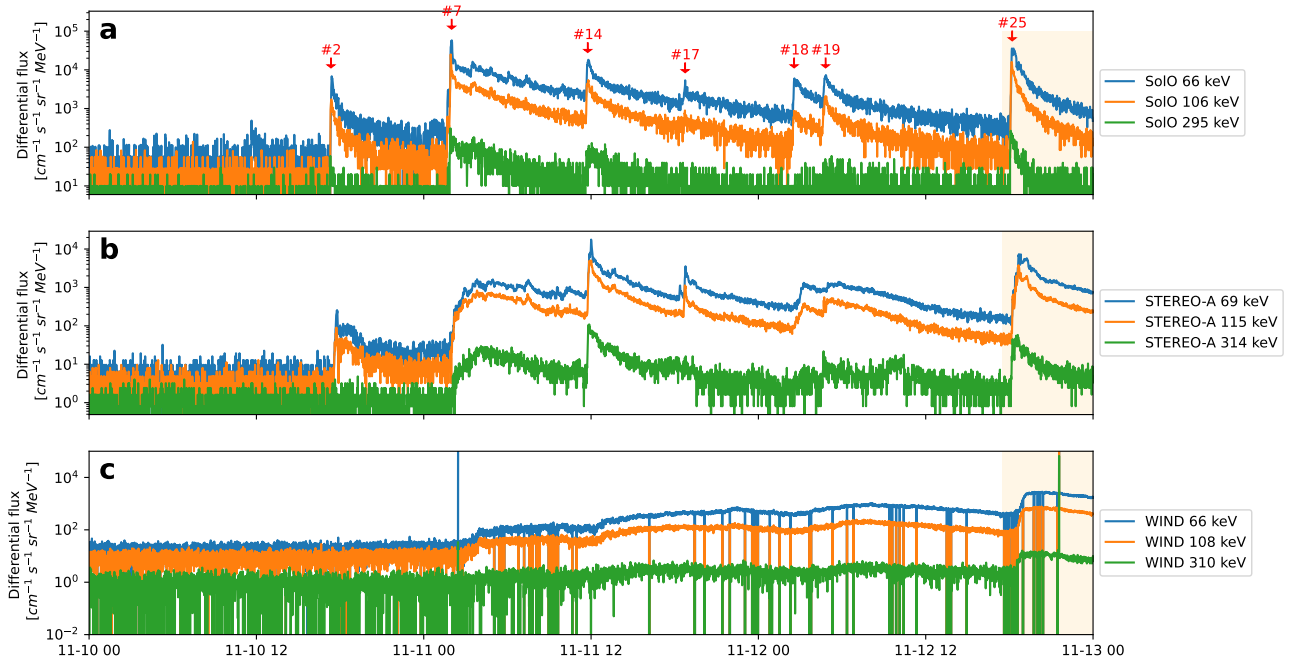

Figure 2. Electron differential flux observed by SolO/EPD (a), STEREO-A/SEPT (b), and WIND/3DP (c). The orange shaded region shows the 2022 November 12 SEE event observed by both EOVSA and SolO/STIX, which is selected for spectral analysis. The seven red arrows with red numbers indicate the SEE events that can be clearly isolated in SolO/EPD's 66 keV channel and are also marked as red in Figures 3(a) and (e).

Figure 3 presents the relationship between the 25 SEEs observed during the period from November 10 to 12 and the corresponding remote sensing observations. SolO/STIX provides comprehensive coverage during this time. The STIX X-ray light curves in three different energy channels are shown in Figures 3(b) and (f). The interplanetary type III radio bursts were recorded by multiple spacecraft, including SolO/RPW and STEREO-A/WAVES, as shown in Figures 3(c) and (g) (the SolO/RPW spectrum is not shown here). Figures 3(d) and (h) show the magnetic longitudinal separation between the different spacecraft and AR 13141. Throughout the period, the separation between SolO and AR 13141 remains less than 20°, reaching a minimum in the early hours of November 12. The magnetic footpoints of STEREO-A and WIND at 1 au gradually approach the active region. The earliest clear enhancement observed by WIND, corresponding to event #7 as marked in Figures 2(a) and 3(a), occurred when WIND's magnetic footpoint had a longitudinal separation of ∼57° from the active region. As the separation becomes smaller and smaller at later times (Figures 3(d) and (h)), this longitudinal separation may be regarded as an estimate for the maximum separation angle for WIND to detect this series of SEE events. During the same time period, PSP's magnetic footpoint is initially close to AR 13141 but moves progressively farther away over time. However, due to data gaps in the PSP observations during the time of interest, the PSP data are excluded from this study. The recorded SEEs across different energy ranges are indicated by vertical dashed lines in Figures 3(a) and (e), most of which show good temporal correlation with the peaks of the Geostationary Operational Environmental Satellite (GOES) light curves.

To better illustrate the relationships between these SEEs and various observational features, we mark the SEEs with different colors to highlight their associations with EUV jets (Figure 3(a); yellow arrows), X-ray flares (Figure 3(b); red arrows), and type III radio bursts (Figure 3(c); green arrows). By closely examining the EUV images from the Atmospheric Imaging Assembly (AIA; J. R. Lemen et al. 2012) on board the SDO (W. D. Pesnell et al. 2012), we found that 24 out of the 25 SEEs are associated with jets, while only one event (marked as #23) does not exhibit a clear jet signature.

Figures 3(b) and (f) show the association of the SEE events with X-ray flares observed by SolO/STIX. Among the 25 SEE events, eight events do not have STIX X-ray imaging data available.[5] The remaining 17 events with X-ray imaging data are indicated by red arrows in Figures 3(b) and (f). The source locations of these X-ray flares are shown in Figure 4. The source images are coaligned with the SDO/AIA 171 Å image at a fixed reference time (17:50 UT on November 11), accounting for solar rotation. The red contours indicate STIX sources associated with SEEs, all of which are exclusively clustered around the recurrent jet region, as shown in Figure 3. In contrast, STIX flares without associated SEEs are distributed not only within the jet region but also in other areas surrounding it. The source locations of STIX flares associated with both EUV jets and SEEs are tightly concentrated within the jet region, suggesting that these SEEs are likely to originate from the region with the recurrent jets.

Furthermore, nearly all SEEs are associated with interplanetary type III radio bursts, except that one event was detected with a delay of more than 10 minutes relative to the corresponding type III burst (marked in gray in Figure 3(c)). We further examine the events reported in Table 1 of D. Lario et al. (2024), specifically those in AR 13141 but without jets/eruptions or type III radio bursts. For these events, no SEEs are detected. The close association of the SEE events with jets and type III radio bursts in this active region suggests that, with good magnetic connectivity to the spacecraft and access to open field lines, the presence of solar jets and type III radio

[5] https://datacenter.stix.i4ds.net/

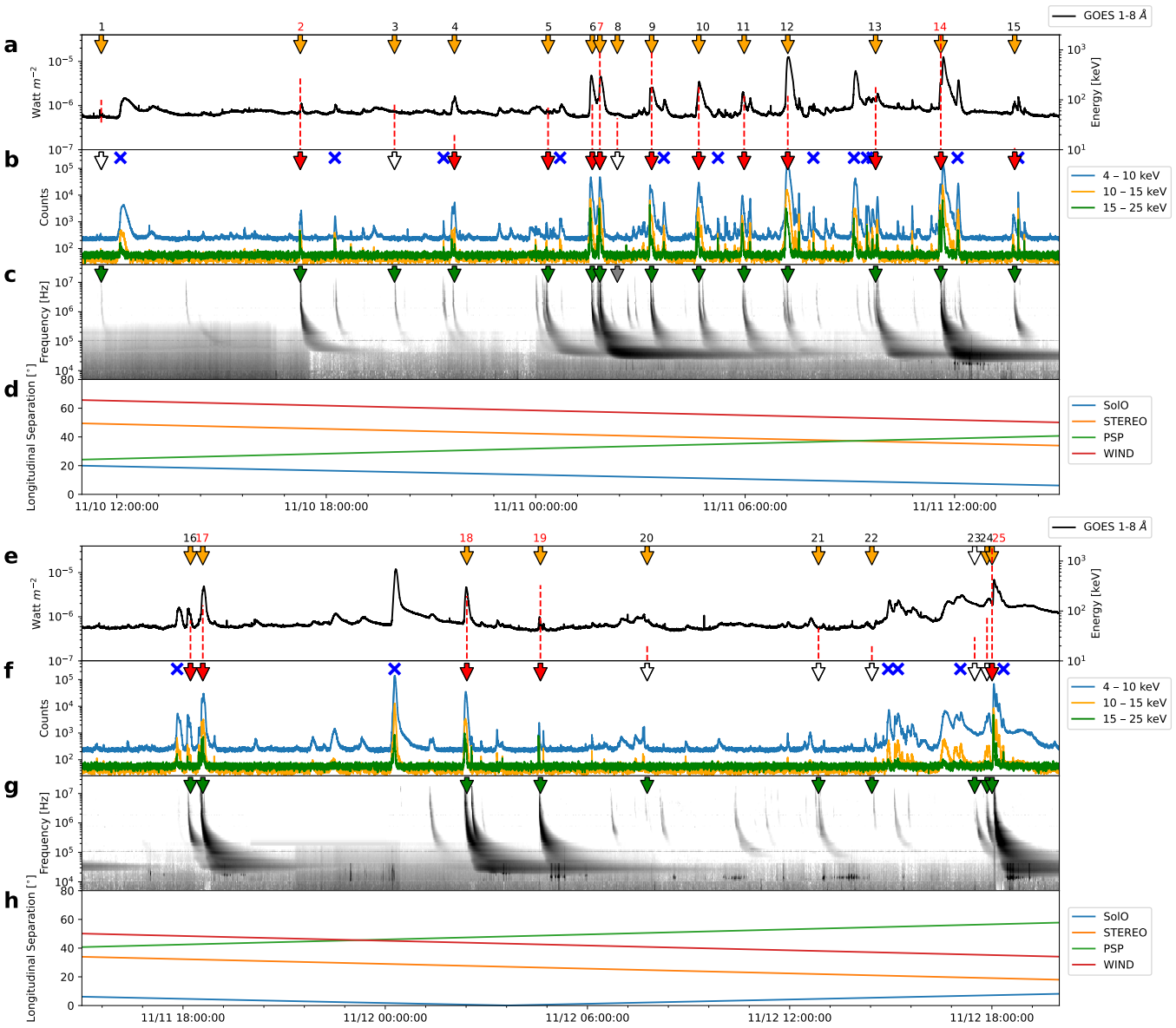

Figure 3. Relationship between the SEE events and GOES, STIX, and type III radio bursts during the period between 2022 November 10 at 11:00 UT and 2022 November 12 at 20:00 UT. The arrows labeled 1–25 indicate the times of the 25 SEE events identified by D. Lario et al. (2024), among which seven marked as red can be clearly identified in the 66 keV channel observed by SolO, shown as red arrows in Figure 2. (a) GOES SXR light curve. The red dashed lines correspond to the SEE events reported by D. Lario et al. (2024), with the vertical heights representing the energy range of the SEEs. The arrows with (without) orange color mark the SEEs associated with (not associated with) the EUV jets. (b) SolO/STIX light curve at three different energy channels. Red arrows indicate SEEs associated with X-ray flares that have corresponding STIX imaging data, while uncolored arrows mark SEEs without available STIX imaging data. Blue cross markers indicate STIX flares with imaging data that are not associated with SEEs. (c) Interplanetary type III radio bursts recorded by STEREO-A/WAVES. Green arrows indicate SEEs associated with type III radio bursts. All the SEE events but one (marked with a gray arrow) are associated with type III radio bursts. (d) Magnetic longitudinal separation between AR 13141 and SolO, PSP, WIND, and STEREO-A. (e)–(h) correspond to the same quantities as (a)–(d) but are presented over a different time interval.

bursts can be effectively considered a necessary condition for the detection of SEEs.

3. The 2022 November 12 Event

In Section 2, we have established that the recurrent jets at the edge of AR 13141 have excellent spatial and temporal correlation with the SEE events observed by SolO. They also have direct magnetic connectivity to the spacecraft and access to open field lines. To further elucidate the relation between the HXR/microwave-emitting energetic electrons near the solar surface and those that escaped to interplanetary space, in this section, we will focus on a particular SEE-associated jet event that occurred on 2022 November 12 around 18:03 UT, with comprehensive coverage by multiple instruments providing multiwavelength remote sensing observations in microwave, (E)UV, and X-rays, together with in situ measurements made by multiple spacecraft including SolO, WIND, and STEREO-A.

3.1. Jet Driven by an Erupting Minifilament

The solar counterpart of this SEE event is classified as a C6.6-class flare accompanied by an EUV jet observed by the GOES (H. A. Garcia 1994) spacecraft. Figures 5(a)–(c) show the soft X-ray (SXR), microwave, and HXR light curves from

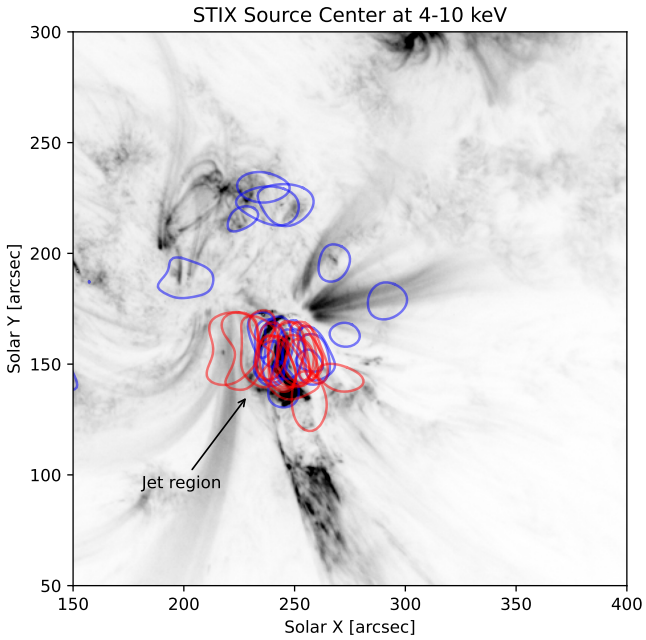

Figure 4. STIX sources at the 4–10 keV energy range (50% contour of the maximum intensity at each energy channel), overlaid with the SDO/AIA 171 Å image at 17:50 UT on 2022 November 11. The AIA field of view is the region corresponding to the black box shown in Figure 1(b). The red contours correspond to STIX sources associated with SEEs, while the blue contours correspond to STIX sources without SEEs. All STIX sources have been rotated to the SDO/AIA viewing perspective.

GOES, EOVSA, and STIX, respectively. Figures 6(a)–(d) show the jet eruption process observed by multiple channels of SDO/AIA. Just before the eruption, a minifilament, appearing as dark material, marked by the white arrow, is visible in the SDO/AIA 304 Å channel. About 2 minutes later, the filament begins to rise and erupt outward toward the southwest direction, shown in Figure 6(b). At the peak of the HXR and microwave light curves around 18:02:19 UT, two miniribbons appear on the northern side, indicated by two white arrows in Figure 6(c). The 30% contours of the 304 Å image, representing the ribbons, are overplotted on the radial magnetic field map in Figure 6(f). At about 18:04:42 UT, plasma materials have been ejected, forming the jet spire from the northeast to the southwest, as shown in panel (d). The preeruption dark filament marked by the yellow solid line is identified from the dark feature located between regions of opposite magnetic polarity, as shown in panel (a). The observed morphology in our case, featuring an erupting minifilament from the base region, is consistent with the "blowout jet" scenario (R. L. Moore et al. 2010; A. C. Sterling et al. 2015). The yellow lines in Figure 6(h) represent magnetic field lines derived from a potential force-free field extrapolation model (using the codes available in the `GX_Simulator` package under `SSWIDL`; A. Stupishin 2020; G. M. Nita et al. 2023). The field lines toward the south correspond to the geometry of the jet spire shown in Figure 6(d).

The temporal evolution of the event during the flare, as observed by the SDO/AIA 304 Å channel, is shown in Figure 7. Around the HXR and microwave peak, a bright blob appears (marked by the white arrow in panels (b)–(d)) and quickly erupts along the direction of the jet spire. Such a small-scale eruption likely represents a portion of the destabilized filament near its northern footpoint, which erupts first to induce the two conjugate miniribbons in a fashion similar to the standard two-ribbon flare picture. In this case, magnetic reconnection may occur at a location in a region underneath the eruption, driving the energy release and particle acceleration during the microwave/HXR peak of the event.

Due to SolO's different viewing perspective from Earth, we reproject STIX to match the viewing perspective of the AIA/HMI images. Figures 6(f) and (g) show the STIX sources during the event peak in the 16–28 keV (purple) energy channels. The viewing perspective of SolO/STIX results in a large viewing angle relative to the flare site. The foreshortening effect may lead to compromised resolution in the east–west direction for STIX imaging. Nevertheless, the northern 16–28 keV HXR source appears elongated between the positive and negative magnetic polarities and is aligned with the northern miniarcade, shown in green.

EOVSA observed the full event in the 1–18 GHz microwave range at a 1 s time cadence (D. E. Gary et al. 2018). We perform imaging spectroscopy in the frequency range from 2.55 to 11.32 GHz, which exhibits a strong signal-to-noise ratio. The EOVSA images have been calibrated, self-calibrated, and reconstructed using the `tclean` task available in the CASA package (J. P. McMullin et al. 2007). The frequency-dependent circular restoring beam has a size of $80''/\nu_{\rm GHz}$, where $\nu_{\rm GHz}$ is the frequency in GHz. Figure 6(g) shows the EOVSA multi-wavelength microwave sources at the peak time (~18:02:22 UT), with blue to red color contours representing decreasing frequencies. The microwave sources appear to be located close to the northern HXR source. Particularly, the higher-frequency sources (cyan to blue colors) display an arcade-like shape bridging the conjugate miniribbons, which are located next to (or just above) the miniarcade seen in EUV.

Here, we summarize the multiwavelength observations and illustrate our understanding of the event geometry in Figure 8. Before the event, the minifilament lies near and slightly above the polarity inversion line, marked by the gray dashed lines. During the initiation of the event, the minifilament is activated, with its northern end undergoing a more rapid rise. Similar to the standard two-ribbon flare scenario, the rising filament induces magnetic reconnection underneath it, leading to the formation of a mini-postflare arcade bridging the two conjugate miniribbons seen in EUV (see Figures 6(c) and (d)). Despite a compromised angular resolution due to foreshortening, the location of the two EUV miniribbons agrees with the elongated northern HXR source, suggesting the presence of precipitated nonthermal electrons as a result of the reconnection. The location of the southern HXR source agrees with the southern end of the preeruption minifilament (see Figure 6(f)), which may be due to the transport of nonthermal electrons along the magnetic flux rope toward its footpoints (e.g., B. Chen et al. 2020b; M. Z. Stiefel et al. 2023). Meanwhile, the high-frequency microwave sources, which display an arcade-like shape, are located close to and seemingly just above the EUV miniarcade (cyan and blue contours in Figure 6(g)). The low-frequency microwave source, on the other hand, extends beyond and above the miniarcade toward the presumed reconnection site. This observed signature is analogous to previous observations of major eruptive flares in which microwave sources are present in the above-the-loop-top region (B. Chen et al. 2020a; S. Yu et al. 2020). They have been suggested to be the signature of nonthermal electrons accelerated and trapped in the "magnetic

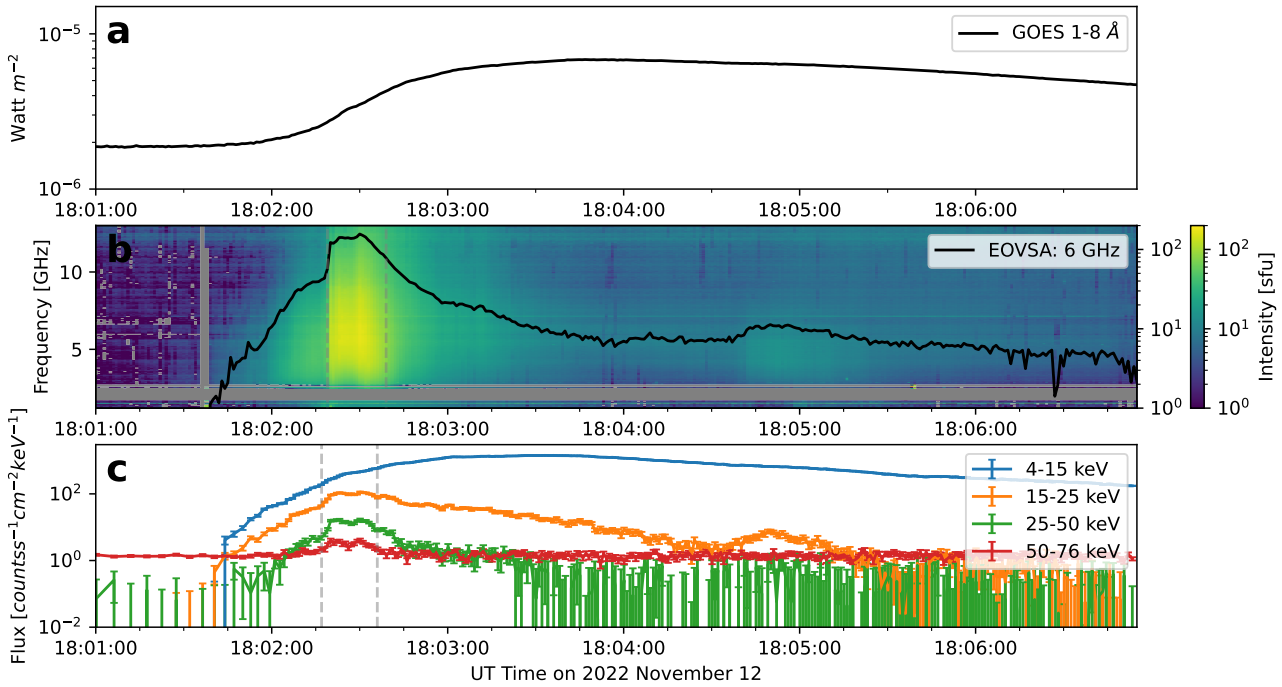

Figure 5. Overview of the time history of the 2022 November 12 jet event. (a) GOES SXR light curve. (b) Total-power radio dynamic spectrum in the microwave range observed by EOVSA, with the black curve representing the light curve at 6 GHz (the data gap region is indicated by gray shading). The gray dashed lines indicate the FWHM duration of the 6 GHz microwave emission, which lasts 21 s. (c) STIX-observed HXR light curves at different energy channels. The pre-flare background has been subtracted. The gray dashed line indicates the FWHM duration of the 25–50 keV burst, which lasts 19 s.

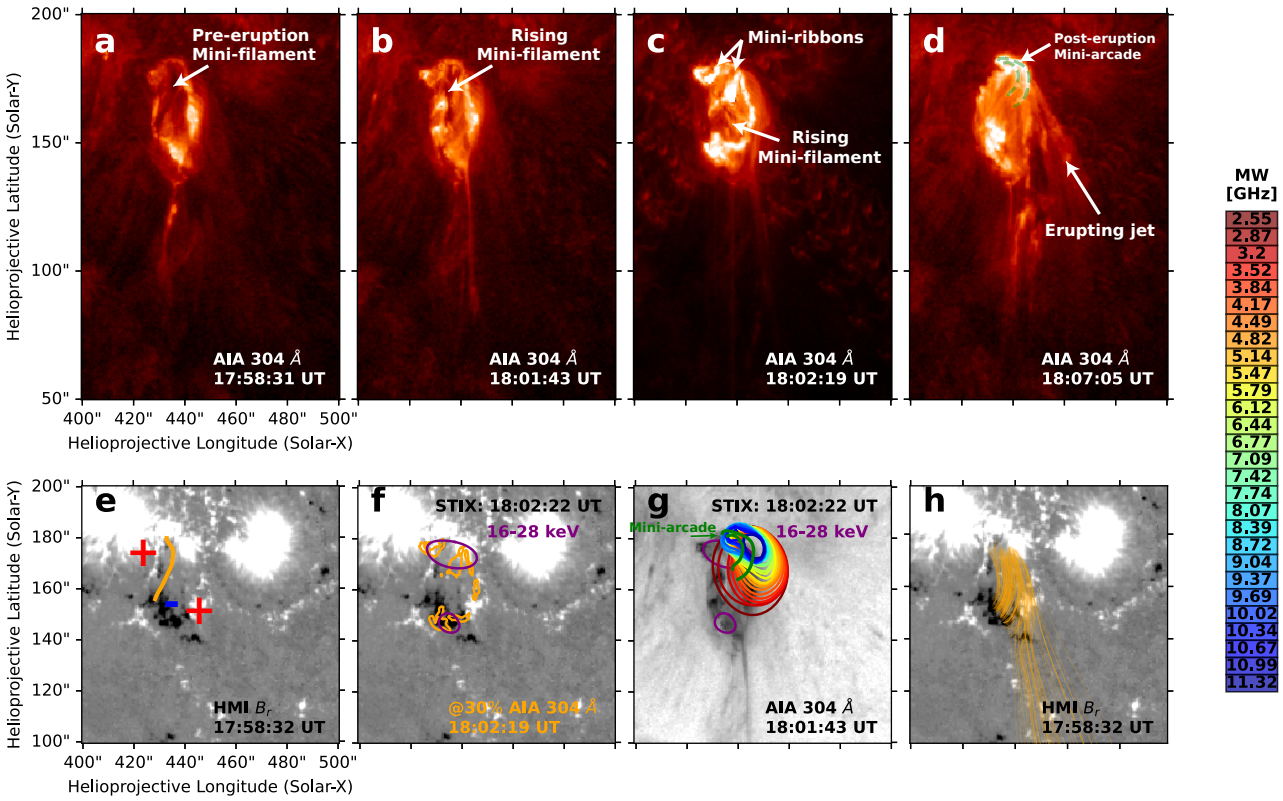

Figure 6. Morphology and evolution of the 2022 November 12 jet event. (a)–(d) Time-series EUV images observed by the SDO/AIA 304 Å band. (e) SDO/HMI radial field magnetogram at 17:58:32 UT. The orange curve represents the minifilament feature identified in panel (a). (f) The background shows the SDO/HMI radial field magnetogram at 17:58:32 UT. The orange contours represent 30% of the peak value from the SDO/AIA 304 Å band at 18:02:19 UT in (c). The STIX nonthermal (16–28 keV) sources, shown in purple with 70% contours, have been reprojected onto the SDO/AIA viewing perspective. (g) Microwave sources with 50% contours at different frequency channels, represented by different colors, overlaid on the SDO/AIA 304 Å image. The purple contours represent the same STIX 16–28 keV sources as in panel (f). The green curve, derived from the green dashed lines in panel (d), shows the miniarcade structure observed in AIA. (h) Selected field lines (yellow curves) derived from a potential magnetic field extrapolation model overlaid on the SDO/HMI radial field magnetogram.

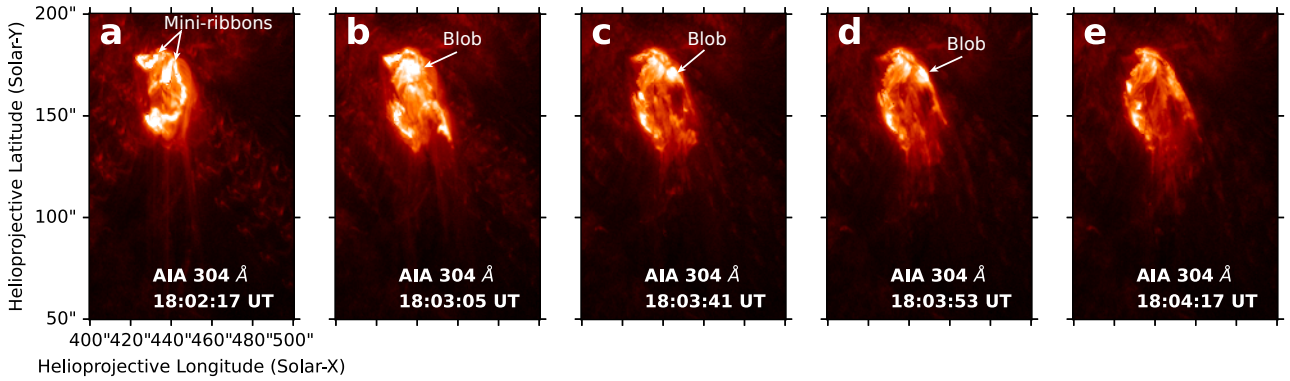

Figure 7. (a)–(e) Temporal evolution of the 2022 November 12 jet event featuring an erupting blob along the jet spire. The two white arrows in (a) indicate the two miniribbons. The white arrows in (b)–(d) indicate the erupting blob.

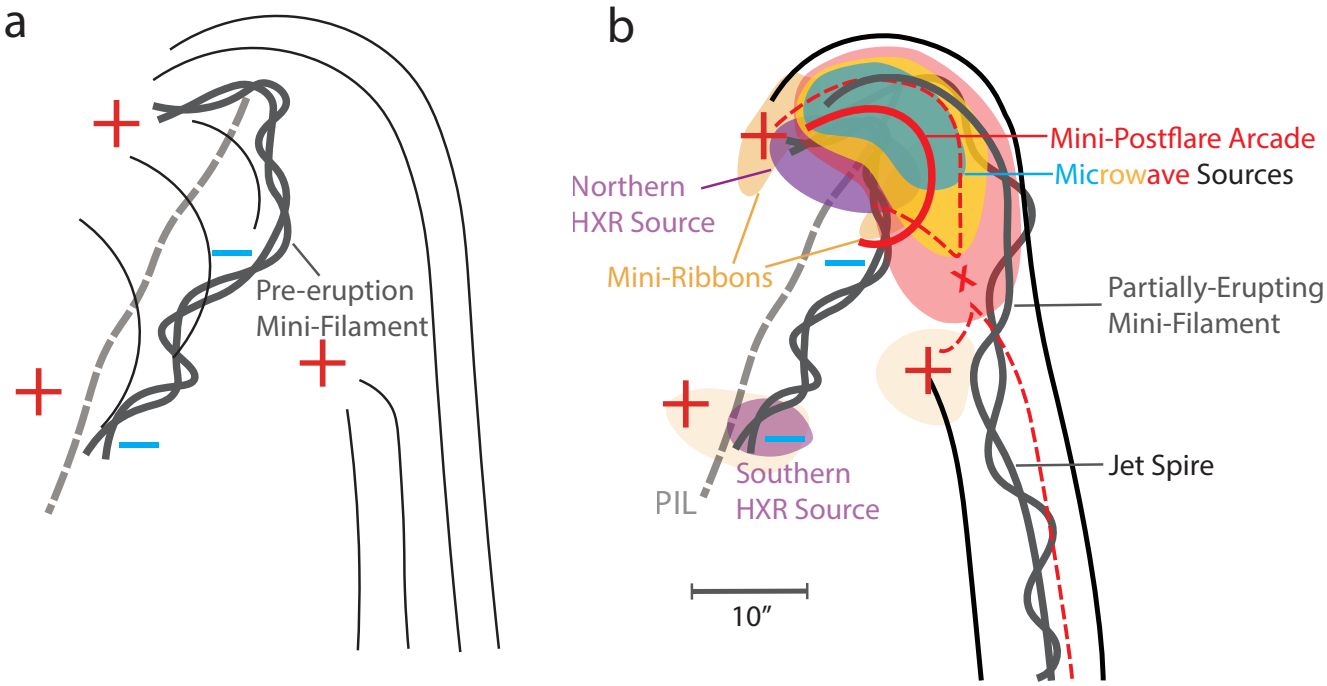

Figure 8. An illustration of the physical scenario of the blowout jet event. (a) Initially, a minifilament lies close to the polarity inversion line. The black curves illustrate the preeruption magnetic field lines. (b) During the event, magnetic reconnection occurs underneath the partially erupting filament material, leading to energy release and particle acceleration. A pair of conjugate miniribbons appears at the footpoint of the mini-postflare arcade, coinciding with an elongated HXR source that may be underresolved due to the foreshortening effect. High-frequency microwave sources (depicted by the blue shaded region), which display an arcade-like shape, are located above the mini-postflare arcade, while the low-frequency microwave sources (depicted in yellow–pink color) extend upward and display a cusp shape toward the presumed magnetic reconnection site. The locations of the microwave sources are analogous to those observed in the above-the-loop-top region in major flares. The remote HXR footpoint may correspond to the southern footpoint of the minifilament. Meanwhile, jet material flows along the field lines toward the southwest.

bottle" structure in this region (B. Chen et al. 2024). The energy release induced by the reconnection drives a mixture of heated coronal plasma and cool filament material flowing along the open field lines, forming the observed jet spire toward the southwest. Complex internal and external magnetic reconnection can also occur during the filament eruption, enabling energetic electrons to escape into interplanetary space along the open field lines.

3.2. Microwave and HXR Spectral Analysis

Microwave data recorded by EOVSA in this event enable us to perform spatially resolved spectral analysis at different locations. Here we select microwave spectra derived from one slit, starting from near the northern footpoint and extending southwest, as indicated by the black dashed line in Figure 9(a). To ensure sufficient signal-to-noise for spectral analysis, we choose frequency channels where the peak flux is at least 3 times higher than the rms of a background source-free region. The spatially resolved brightness temperature spectrum derived from the selected slit is shown in Figure 9(b), with the horizontal axis indicating the distance along the starting point of the slit (near the northern footpoint) and the vertical axis representing the microwave frequency. Three representative spectra, taken at distances of 2.″7, 14.″0, and 23.″6 from the northern starting point (marked by the red dashed lines in Figure 9(b) and the red circles in Figure 9(a)) are shown in Figures 9(c)–(e).

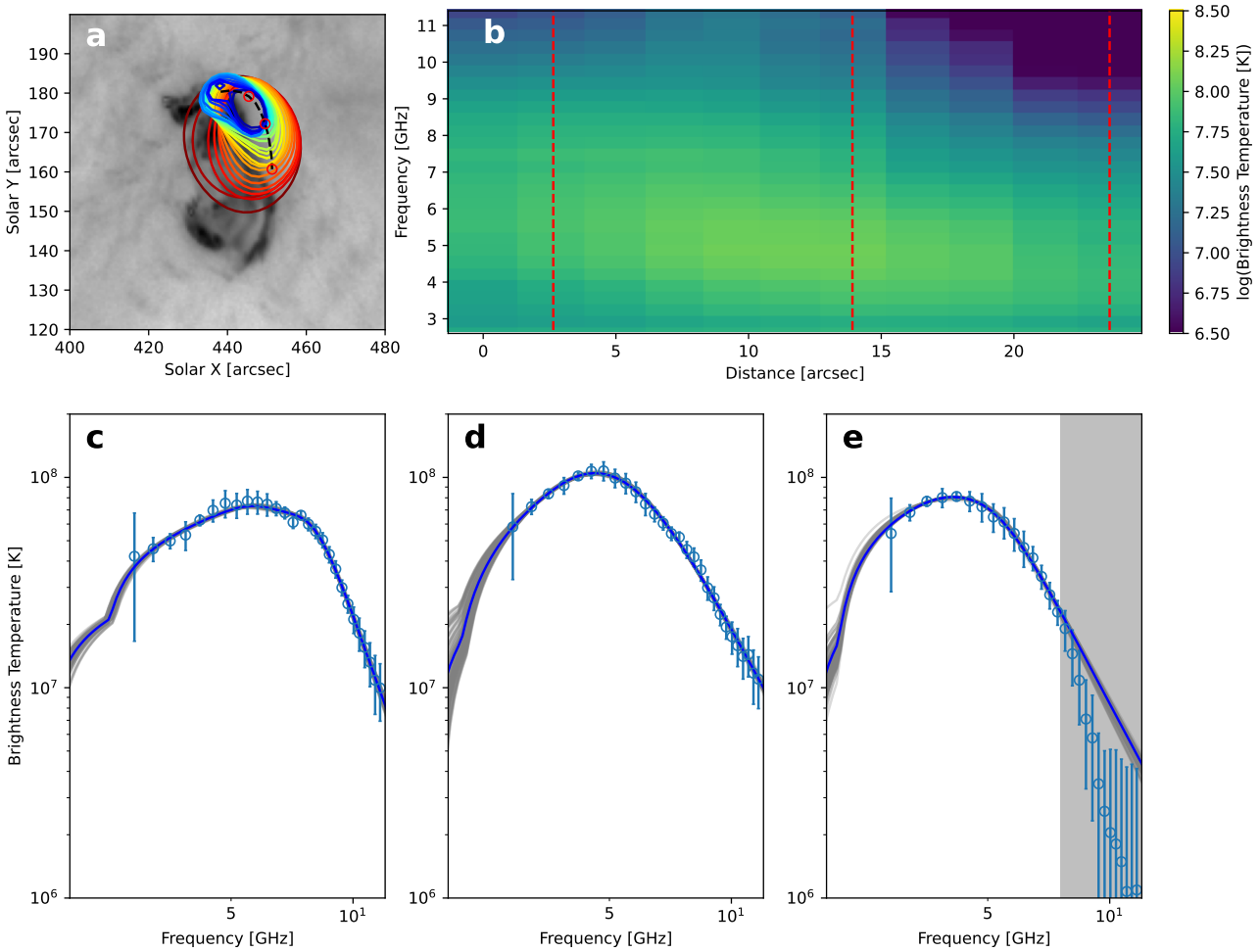

Figure 9. Microwave imaging spectroscopy during the peak of the eruptive jet event at 18:02:22 UT. (a) Microwave sources at different frequency channels (50% contour of the respective maximum) are shown. The black dashed line represents the selected slit to generate the "frequency–distance" spectrogram in (b), in which the *x*-axis shows the distance from the northernmost starting point and the *y*-axis shows the frequency. The red dashed lines in (b), which correspond to the red circles in (a), indicate the three selected representative locations from which the microwave spectra shown in (c)–(e) are derived. The error bars in panels (c)–(e) represent 3 times the rms of the source-free background. The gray curves show the MCMC runs, while the blue curves represent the best-fit results. The gray areas represent the frequency channels with insufficient signal-to-noise values and are therefore excluded from the spectral fitting.

The observed microwave brightness temperature spectrum exhibits a positive slope at lower frequencies. After reaching the turnover frequency, it transitions to a negative slope at higher frequencies. Such a spectral shape is consistent with gyrosynchrotron radiation (G. A. Dulk 1985), in which the low-frequency, positive-slope portion of the spectrum is dominated by emission in the optically thick regime and the high-frequency, negative-slope portion is due to optically thin emission. Here, we adopt the fast gyrosynchrotron codes developed by G. D. Fleishman & A. A. Kuznetsov (2010) and fit the spectra under the assumption of a homogeneous source with a power-law nonthermal electron distribution. The background plasma temperature is fixed to 3 MK. The low-energy cutoff of the nonthermal electron distribution is set to 20 keV, and the high-energy cutoff is set to 10 MeV.[6] The column depth is fixed at 15″, estimated using the microwave source size at ∼5 GHz. The parameters used for fitting are the power-law spectral index of the differential electron density distribution δ', the total nonthermal electron density $n_{\rm nth}$ above the low-energy cutoff, the thermal plasma density $n_{\rm th}$, the magnetic field strength B, and the angle between the line of sight and the magnetic field vector θ. The fitting procedure is performed using the Markov Chain Monte Carlo (MCMC) method in order to find the global minima in the multi-parameter space (following B. Chen et al. 2020a).

The best-fit source parameters and their uncertainties are presented in Figures 10(a)–(c). The magnetic field strength B is at its maximum near the northern footpoint (0″–5″ from the starting point), reaching ∼500 G, and gradually decreases toward the southwest. The nonthermal electron density $n_{\rm nth}$ reaches its maxima near both the northern footpoint and the above-the-loop-top region (at a distance of 12″ from the northern footpoint) with a value of $\gtrsim 3.0 \times 10^6\,{\rm cm}^{-3}$. It then gradually decreases to $\sim 3.2 \times 10^4\,{\rm cm}^{-3}$ toward the southwest, or <1% of its maximum value.

Next, we conduct HXR spectral analysis using a composite model consisting of an isothermal component and a nonthermal thick-target component with a power-law electron distribution using the `OSPEX` package included in the `SSWIDL` software suite (R. A. Schwartz et al. 2002). The observed X-ray spectrum and fitting results are shown in Figure 11. The best-fit power-law spectral index of the differential electron flux distribution δ is 4.06 ± 0.08, and the low-energy

[6] We note that the spectral fit results are insensitive to the selected value of the high-energy cutoff, as long as it is above a few hundred keV.

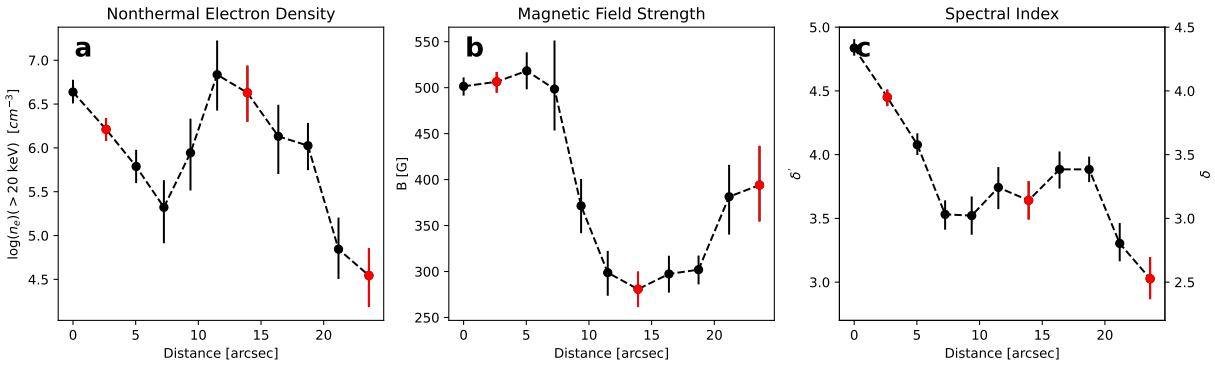

Figure 10. Best-fit values for total nonthermal electron density n_e (>20 keV), magnetic field strength B, and power-law index of the nonthermal electron density distribution δ' from the spatially resolved microwave spectral analysis. The error bars shown in the plots are estimated using the 1σ variance from the MCMC runs. The three red points in each panel indicate the representative points for spectral analysis in Figure 9.

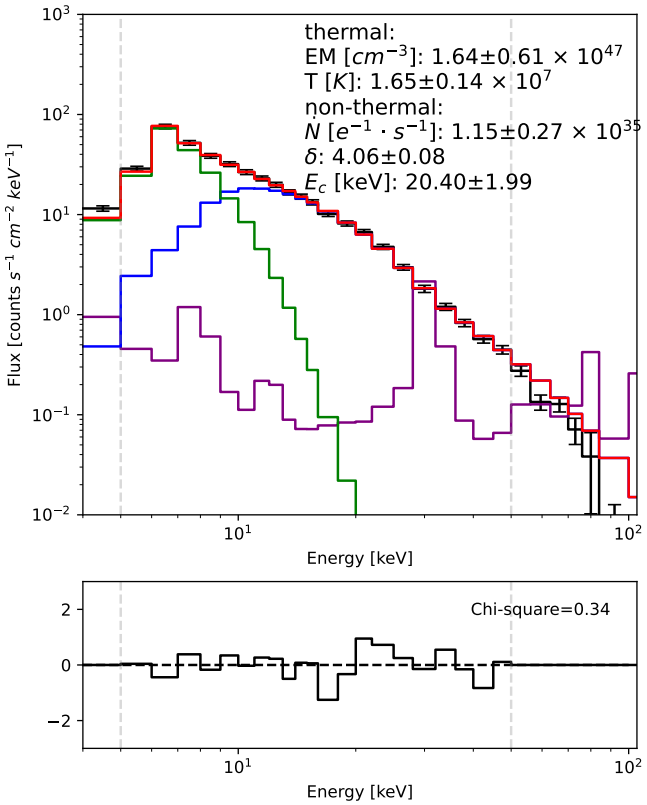

Figure 11. X-ray spectral fitting results based on SolO/STIX observations at 18:02:22 UT integrated over 10 s. The black curve shows the data. The blue, green, and red curves show the best-fit nonthermal (assuming a thick-target model) component, the isothermal component, and the two components combined, respectively. The purple curve represents the background. The energy range selected for fitting is between 5 and 50 keV, as indicated by the gray dashed lines. The best-fit parameters are listed in the top right corner of the plot (EM: emission measure. T: plasma temperature. $\dot{N}$: total nonthermal electron rate. δ: spectral index of the nonthermal electron flux distribution. E_c: low-energy cutoff of the nonthermal electron distribution.

cutoff E_c is 20.4 ± 1.99 keV. The total electron rate $\dot{N}$ is 1.15 ± 0.27 × 10^{35} s^{-1}.

The total number of accelerated electrons produced during the jet event can be estimated using both the microwave and HXR spectral analysis results. For HXR-constrained electron numbers, we use three selected energy channels to calculate the total nonthermal electron rates above E_s = 30, 50, and 120 keV, which can be derived using the following equation: $\dot{N}_{>E_s} = \dot{N}_{>E_c}\left(\frac{E_c}{E_s}\right)^{\delta-1}$, where E_c = 20.40 keV is the low-energy cutoff returned from the HXR spectral analysis (Figure 11). The total number of HXR-derived nonthermal electrons in the three selected energy channels is calculated using the relation $N^{\rm HXR}_{>E_s} = \dot{N}^{\rm HXR}_{>E_s}\tau_{\rm HXR}$, where the duration $\tau_{\rm HXR}$ is taken to be 19 s, based on the full width at half-maximum (FWHM) duration of the 25–50 keV light curve. The results are shown in the first row of Table 1.

Table 1
Total Number of Energetic Electrons

	>30 keV [$\times 10^{32}$]	>50 keV [$\times 10^{32}$]	>120 keV [$\times 10^{32}$]
$N^{\rm HXR}$	6713.2 ± 2557.9	1406.2 ± 543.5	96.5 ± 39.1
$N^{\rm MW}$	3323.2 ± 3650.6	879.7 ± 1152.8	95.6 ± 141.3
$N^{\rm SEE}$	5.4 ± 3.0	3.2 ± 1.7	1.0 ± 0.3
$N^{\rm SEE}/N^{\rm HXR}$	0.08%	0.23%	0.97%
$N^{\rm SEE}/N^{\rm MW}$	0.16%	0.36%	0.96%

Note. Total number of energetic electrons above three selected energy thresholds, 30, 50, and 120 keV, as derived from HXR, microwave (MW), and in situ SEE observations.

For the microwave estimation, we derive the total number of microwave-emitting electrons above the selected energy channel E_s using the following formula:

$$N^{\rm MW}_{>E_s} = \tau_{\rm MW} \cdot A \cdot \int_{E_s}^{E_{\rm max}} v_e \cdot f_e \, dE. \quad (1)$$

Here, $\tau_{\rm MW}$ is the duration of the microwave emission, which is 21 s based on the FWHM of the 6 GHz light curve. A is the cross-section area of the microwave source, set to be $15'' \times 15''$, v_e is the electron velocity, and f_e is the differential electron density distribution following a power-law form ($f_e = dn_e/dE \propto E^{-\delta'}$). With the best-fit parameters derived from the microwave spectra, similarly, we obtain the total number of microwave-emitting nonthermal electrons above 30, 50, and 120 keV. The results are shown in the second row of Table 1. The total number of microwave-emitting electrons is consistent with that of the HXR-emitting electrons, which are of the same order of magnitude.

3.3. Multispacecraft In Situ SEE Measurements

On 2022 November 12, in addition to SolO/EPD, both WIND/3DP and STEREO-A/SEPT detected a significant enhancement in the in situ energetic electron flux (Figure 2). At this time of interest, the magnetic longitudinal separations

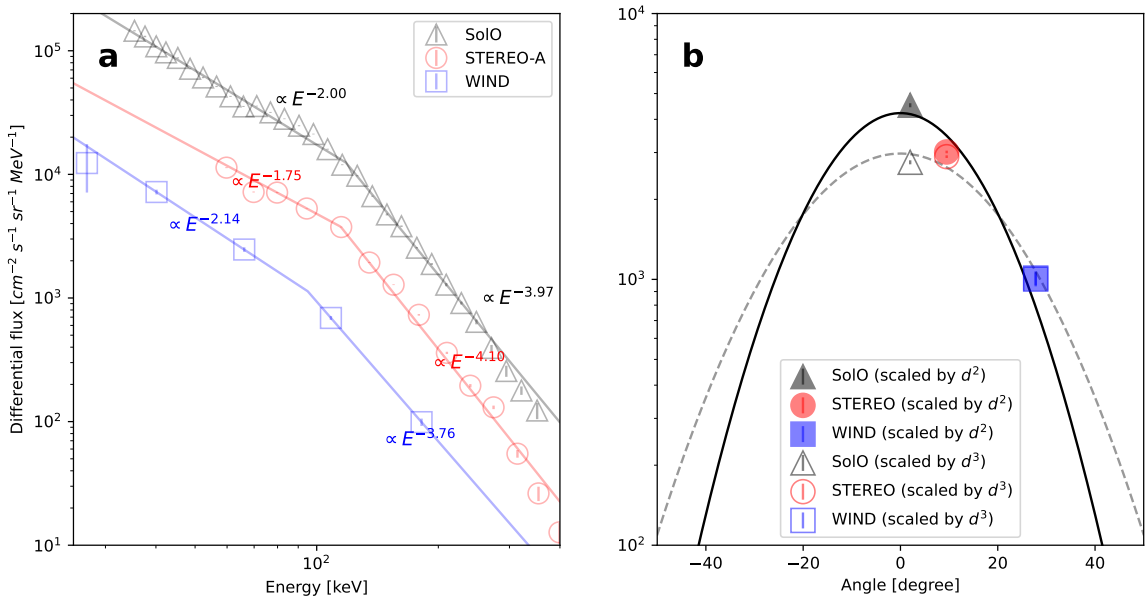

Figure 12. (a) In situ energetic electron spectra from the 2022 November 12 SEE event. The triangle, circle, and square markers with error bars indicate the peak energetic electron spectra observed by SolO, STEREO-A, and WIND, respectively. The length of the error bars represents the 3σ uncertainty of the event background (most are too small to see). The solid lines represent the spectral fitting results using a double power-law model. (b) Peak 120 keV SEE flux as a function of magnetic longitudinal separation from the jet region of the event observed by SolO (black), STEREO-A (red), and WIND (blue). Filled and open symbols show the results scaled using the $F \propto d^{-2}$ and $F \propto d^{-3}$ relation, respectively. Solid and dashed curves show the respective Gaussian fit results.

between the active region and SolO and STEREO-A were both less than 20°. As discussed in Section 2, to enable an accurate comparison of the peak flux among different spacecraft, here we adopt the sector-averaged flux across different viewing directions for the electron spectral analysis. In Figure 12(a), we show the electron spectra measured by the three spacecraft derived from the peak electron flux during this event. The electron flux spectra are fitted using a broken power-law distribution. For the WIND observations, only five energy channels show a clear signal. Therefore, the break energy was fixed in the range of 100–120 keV according to the fitting results from STEREO-A and SolO observations. The spectral fitting results from the three spacecraft consistently indicate that the low-energy spectral indices are approximately 2, while the high-energy spectral indices are around 4, with a break energy of 100–120 keV.

In addition, the three spacecraft located at widely spread longitudinal angles also allow us to estimate the angular distribution of the SEE event. Here, we fit the peak flux at 30, 50, and 120 keV, using the data observed by SolO, WIND, and STEREO-A, with a Gaussian function (following, e.g., I. G. Richardson et al. 2014; R. D. Strauss & H. Fichtner 2015; H. Xie et al. 2019). In addition to the different longitudinal separations, the peak flux is strongly affected by the spacecraft's radial distance from its source d. In our case, SolO is located at 0.61 au from the Sun, whereas STEREO and WIND are approximately 1 au away. To normalize the electron flux obtained by SolO to a common heliocentric distance of 1 au, we first scale the observed electron flux by a factor of d^{-2}, assuming free ballistic propagation. The scaled peak fluxes at 120 keV are shown in Figure 12(b) as black symbols. The solid black curve represents the fitted Gaussian function. The derived FWHM of the SEE angular distribution using the multispacecraft measurements is 28°, which is broadly consistent with the maximum separation angle of ∼57° for WIND to detect an SEE event (see Section 2), as well as previous statistical results (R. P. Lin 1974). Some studies show that a d^{-3} dependence may be more likely due to transport effects (L. Rodríguez-García et al. 2023). The gray dashed line in Figure 12(b) represents the fitted Gaussian function using the peak flux scaled by the d^{-3} relation instead. In this case, the FWHM of the best-fit Gaussian function is 40°. Owing to the similar spectral shapes observed by the three spacecraft, similar results for the angular extent can be derived if we choose other energy channels for this analysis.

The in situ SEE spectra and estimated angular extent are, in turn, used to estimate the total number of electrons that escaped into interplanetary space (see, e.g., T. James et al. 2017). By integrating the event duration of ∼2.5 hr, defined as the period during which the flux at least exceeds 3σ above the background, the total numbers of energetic electrons above 30, 50, and 120 keV that manage to escape into interplanetary space are shown in the third row of Table 1. Compared to the estimated total number of HXR- and microwave-emitting electrons near the solar surface, the ratio of escaped electrons to those near the solar surface is between 0.1% and 1%. These values are extremely small and are consistent with previous findings.

4. Discussion and Conclusion

In this paper, we started from the survey presented by D. Lario et al. (2024) on a series of SEE events occurring from 2022 November 9 to 2022 November 14 incorporating both in situ measurements and multiwavelength remote sensing observations. We placed a special focus on 25 SEE events originating from AR 13141, considering its favorable magnetic connectivity to the SolO spacecraft. We found the following:

1. Nearly all 25 SEEs are associated with interplanetary type III radio bursts with only one event showing a time delay.

2. Twenty-four out of the 25 SEEs are related to solar jets or eruption processes.
3. Seventeen out of the 25 SEEs with available X-ray imaging data from SolO/STIX are concentrated in a distinct recurrent jet region located at the southwest edge of AR 13141 that features mixed polarities.
4. The recurrent jet source region has a very small ($<20^\circ$) longitudinal separation between the ballistically projected footpoints of SolO. These footpoints are located close to a narrow region with direct access to open field lines, favorable for particles to escape to interplanetary space.

The above findings strongly suggest that jet events in this specific region, which are accompanied by interplanetary type III radio bursts, share a common origin with the corresponding in situ SEE event. This connection enables a direct comparison of the energetic electron population near the solar surface with the population that enters interplanetary space. Next, we focus on a specific jet-associated SEE event that occurred on 2022 November 12 at around 18 UT that has excellent coverage by a suite of remote sensing and in situ instruments including SolO, EOVSA, SDO, WIND, and STEREO-A. In particular, joint HXR and microwave imaging spectroscopy offered by SolO/STIX and EOVSA provides comprehensive diagnostics of the nonthermal electron distribution over a wide energy range. Meanwhile, in situ measurements made by multiple spacecraft (SolO, WIND, and STEREO-A) located at various heliographic longitudes and distances offer a great opportunity to constrain the angular distribution of energetic electrons entering interplanetary space, derived to have an FWHM angle of 28° assuming free propagation.

The in situ SEE spectra observed by three different spacecraft at different heliocentric longitudes all exhibit a broken power-law distribution with similar power-law indices and break energies around 100–120 keV. Only the absolute flux varies with each spacecraft's angular separation from the source. This spectral uniformity across longitudes suggests that the broken power-law distribution may be an intrinsic property of the accelerated SEE population entering interplanetary space.

For the HXR spectral analysis ($\sim$20–100 keV), which serves as a remote diagnostic of energetic electrons near the solar surface, we used a single power-law distribution. A broken power law was not employed because the data show no sign of a break in this range. For microwave spectral analysis, we also adopted a single power-law form for the nonthermal electron distribution mainly because the microwave data alone do not have sufficient constraints for determining a more complicated distribution with additional free parameters (such as a broken power-law form; see, however, B. Chen et al. 2021 for a successful example when both microwave and HXR data could be utilized to jointly fit the same nonthermal coronal source). Nevertheless, the spatially resolved microwave spectral fitting results suggest that the spectral index of the microwave-emitting electrons near the footpoint (the first point in Figure 10(c)) is $\delta \approx \delta' - 0.5 \approx 4.0$, consistent with the HXR fitting results. A harder spectrum of $\delta \approx 3.1$ is observed near the loop top (at a distance of $\sim 15''$ in Figure 10(c)). A harder electron spectrum at the loop top has also been reported in the literature (e.g., J. E. R. Costa & A. C. Rosal 2005; S. Mondal et al. 2024), which may be attributed to more effective trapping of high-energy electrons in the coronal acceleration region due to turbulent pitch-angle scattering (E. P. Kontar et al. 2014; S. Musset et al. 2018). Interestingly, the energetic electron spectrum in the region further away from the loop-top region close to the base of the EUV jet spire, despite having a much smaller number density, exhibits an even harder spectrum with $\delta \approx 2.5$, approaching the spectral index derived from in situ observations in the 30–100 keV range.

Next, in Section 3, we have estimated the total number of HXR/microwave-emitting nonthermal electrons near the solar surface and compare it to those entering the interplanetary space measured by multispacecraft in situ measurements. We notice that the estimation of the total number of escaping electrons based on in situ measurements can be strongly affected by the angular extent of nonthermal electrons entering interplanetary space. For single-spacecraft measurements, this angular extent is essentially unknown and has to be assumed. A nominal angular width of 30° is often assumed (e.g., S. Krucker et al. 2007) based on statistical studies of the longitudinal distribution of SEE-associated flare events observed from Earth (R. P. Lin 1974; D. V. Reames 1999). However, if the angular width were larger than the assumed value by a factor of 3, the total number of electrons escaping to interplanetary space could increase by nearly an order of magnitude. Indeed, in one jet event, using microwave imaging spectroscopy observations of a type III radio burst in $\sim$1–3 GHz, M. Wang et al. (2023) reported that the angular extent of the type-III-burst-emitting electrons escaping along open field lines is much broader than the EUV jet spire, reaching $\sim 90^\circ$. In this study, by utilizing observations from three spacecraft located at various longitudinal positions, we have a more robust constraint of the angular extent of the escaping electrons to be from 28° to 40°, thus greatly reducing the associated uncertainties of the derived ratio of escaped versus retained energetic electrons.

Based on the improved constraints discussed above, we conclude that the fraction of energetic electrons that escape into interplanetary space is extremely small, only 0.1%–1% of the microwave/HXR-emitting electrons near the solar surface, consistent with previous reports. As introduced earlier, one interpretation posits that the in situ SEEs originate from an initial acceleration site high in the corona; thereby, they are much lower in number and absence of strong Coulomb collision losses (W. Wang et al. 2021). Our observations do not favor this scenario. Figure 13(a) shows SolO/EPD observations of the SEE spectrogram over a wide energy range from $\gtrsim$10 to 400 keV. Unlike the electron spectral analysis across different spacecraft, to ensure consistency when combining the electron flux measurements from the SupraThermal Electrons and Protons (STEP) instrument with those from SolO/EPD, we adopt the data from sunward sensor viewing directions. A clear velocity dispersion is seen (red dashed line), which is due to higher-energy (or faster) electrons arriving at the spacecraft at an earlier time. Assuming that the electrons propagate along the nominal Parker spiral to SolO, we find that the SEEs are released near the peak time of the microwave and HXR emissions, confirming the common origin of the in situ SEEs and the HXR/microwave-emitting energetic electrons. From there, we extract peak electron fluxes at least 3σ above the background level to represent the in situ electron spectra shown in panel (b). We find that the electrons at low energies (10–40 keV) display a flatter spectrum, which differs from the cases reported by W. Wang et al. (2021), who showed that the same power law extends to extremely low energies ($<$5 keV). The observed spectrum with a flat or positive spectral slope suggests that these low-energy electrons

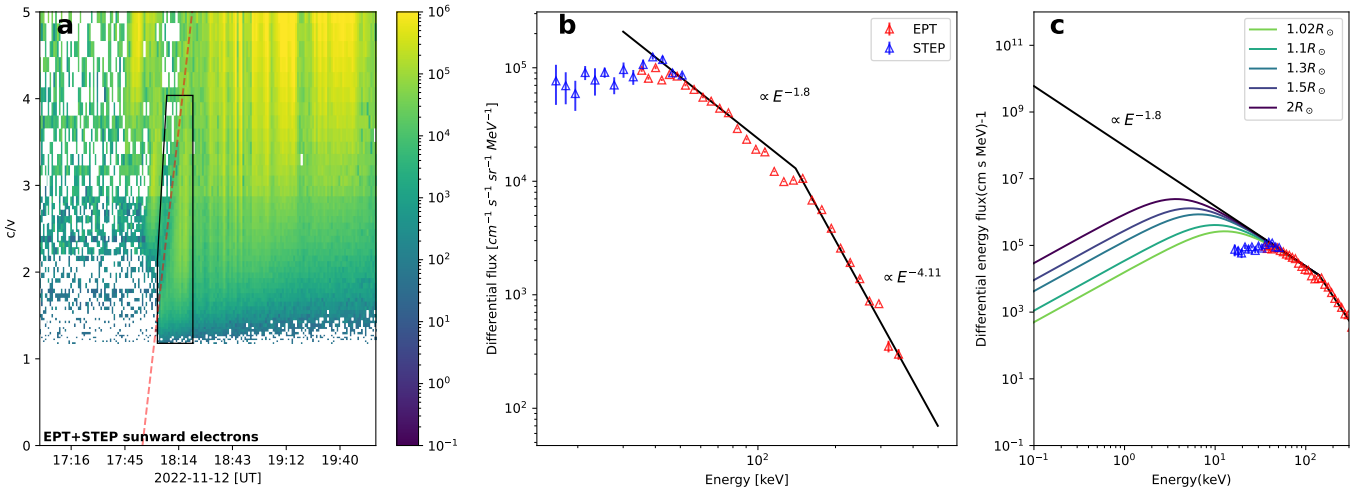

Figure 13. Combined energetic electron spectrum of the 2022 November 12 SEE event, as observed by the sunward detectors of the EPT and STEP instruments on board SolO. (a) Combined SEE spectrogram with background subtracted. The vertical axis represents the energetic electron energy converted to c/v, where c is the speed of light and v is the electron velocity. The black box marks the SEE event of interest, with a clear velocity dispersion feature. (b) Combined EPT and STEP background-subtracted electron spectra with 3σ background error bars derived from the energy-dependent peak times within the black box in panel (a). The blue and red points represent measurements made by STEP and EPT, respectively. (c) Coulomb collision model fits of the observed SEE spectrum. The curves in different colors represent the model electron spectra with different injection heights.

originated from the very low corona and have experienced substantial energy loss during their propagation to the spacecraft.

Following earlier work (R. P. Lin 1985; W. Wang et al. 2021; M. Wang et al. 2023), we model the observed SEE spectrum by injecting energetic electrons from various coronal heights with a power-law distribution with a spectral index of $\delta = 2.0$ up to the observed break energy of 120 keV. They lose energy during their propagation to the spacecraft as a result of Coulomb collisions in an energy-dependent manner. Figure 13(c) shows the modeled electron spectra with different injection heights (1.02, 1.1, 1.3, 1.5, and 2 $R_\odot$) using the same density model as in M. Wang et al. (2023) but with the scaling factor adjusted to 5 times the Newkirk model (G. Newkirk 1967) in the low corona. As expected, the low-energy electron spectrum's turnover energy shifts to higher energies for lower injection heights, as the electrons undergo more Coulomb collision losses. Unlike the cases reported in W. Wang et al. (2021), we find that the observed electron spectrum with a turnover energy of ~40 keV is best described by the model with a very low injection height of $<1.02\ R_\odot$, or $<20''$ above the solar surface, consistent with implications from our remote sensing results (see illustration in Figure 8). We note that, even with a low injection height of 1.02 $R_\odot$, the observed turnover energy is still higher than that modeled assuming free propagation. This implies that the low coronal density may be greater than the adopted model or that electrons experience additional transport effects that increase their effective propagation distance (e.g., E. P. Kontar & H. A. S. Reid 2009; R. D. T. Strauss et al. 2017). Therefore, we conclude that the in situ SEEs in our event likely share a common origin with the HXR- and microwave-emitting electrons near the solar surface but are not involved in the secondary acceleration process.

Another possible interpretation favored by our observations is that the population of upward-propagating electrons is significantly depleted before reaching interplanetary space because of effective trapping in the electron acceleration region presumably located above the miniarcade at the jet base. A promising trapping mechanism may be strong diffusion due to turbulence-induced scattering. For example, previous modeling studies have shown that, with strong diffusion, the nonthermal electron density can be reduced by 2 orders of magnitude at a distance of 10–20 Mm away from the acceleration region (S. Musset et al. 2018; B. Chen et al. 2024). This depletion results in an extremely small ratio of escaping electrons compared to HXR/microwave-emitting electrons. This possibility is strongly supported by our spatially resolved microwave spectral analysis results, which show that the nonthermal electron density is only about 2 orders of magnitude at the southwesternmost point where they enter the open field lines (see Figure 10(a)) compared to its peak value near the mini-postflare arcade. Coincidentally, this drop in density of the nonthermal electrons entering open field lines matches the interplanetary-space-to-solar-surface electron ratio by the same order of magnitude (~1%).

Our observations of the small eruptive jet event are consistent with the scenario proposed by B. Chen et al. (2024) for the gradual phase of a major eruptive solar flare (X8.2 class). In our case, the majority of nonthermal electrons may be accelerated and trapped in the above-the-loop-top region above the mini-postflare arcade, where a high concentration of microwave-emitting nonthermal electrons coincides with a reduced magnetic field strength, referred to as a "magnetic bottle" (B. Chen et al. 2020a). Our results indicate that the region located 10″–15″ from the northern point exhibits these characteristics, including a lower magnetic field strength and a peak in nonthermal electron density. As the distance increases toward the southwest, the nonthermal electron density continuously decreases due to effective trapping in the magnetic bottle region, possibly by turbulence and/or strong magnetic mirroring, resulting in a very small number density of nonthermal electrons (2 orders of magnitude lower than the peak density). The location of these microwave-emitting electrons coincides with the base of the jet spire above the reconnection site, which may find a path to enter interplanetary space via the open field lines, giving rise to a small population of in situ SEEs.

Our study benefits from the selection of a favorable time period, during which a series of SEEs shows a close association with type III radio bursts and solar jets originating from an active region with excellent magnetic connectivity. This association provides us with strong confidence in the origin of these SEEs, allowing us to further investigate their acceleration and transport processes. The joint use of HXR and microwave observations probes a wide range of electron energies, allowing us to minimize the transport effects when comparing with in situ measurements. Additionally, multispacecraft in situ measurements of SEEs provide a tight constraint on the angular distribution of the energetic electrons, giving us a more accurate estimate for the electrons entering interplanetary space. More importantly, the simultaneous microwave imaging spectroscopy capability offered by EOVSA, when complemented by EUV, HXR, and magnetic field data, enables us to spatially resolve the nonthermal electron distribution in the core jet region, allowing us to shed new light on the small escaping electron population problem. In the future, next-generation telescopes, such as the Frequency Agile Solar Radio telescope (B. Chen et al. 2023; D. Gary et al. 2023), with significantly higher dynamic range, sensitivity, and angular resolution, are expected to greatly enhance our understanding of the acceleration and transport of SEE events.

Acknowledgments

The authors thank Andrea Francesco Battaglia for valuable discussions. The authors acknowledge the Solar Orbiter Energetic Particle Detector (EPD) team for their guidance in analyzing the electron data. M.W., B.C., and S.Y. were supported by NSF SHINE grant AGS-2229338 and NASA grants 80NSSC24K1242 and 80NSSC20K1282 to the New Jersey Institute of Technology. J.L. acknowledges NSF grant AGS-2114201 and NASA grant 80NSSC24K0258. H.W. acknowledges NSF grant AGS-2209064 and NASA grants 80NSSC20K1282 and 80NSSC24M0174. M. Wickline acknowledges support by the NSF REU program under grant AGS-2050792 "REU Site: Solar, Terrestrial, and Space Weather Sciences at New Jersey Institute of Technology." The Expanded Owens Valley Solar Array (EOVSA) was designed and built and is now operated by the New Jersey Institute of Technology as a community facility. The EOVSA operations are supported by NSF grants AGS-2130832 and AGS-2436999 and NASA grant 80NSSC20K0026 to NJIT.

ORCID iDs

Meiqi Wang https://orcid.org/0000-0002-2633-3562
Bin Chen https://orcid.org/0000-0002-0660-3350
Mallory Wickline https://orcid.org/0009-0009-0282-4904
Sijie Yu https://orcid.org/0000-0003-2872-2614
Säm Krucker https://orcid.org/0000-0002-2002-9180
Jeongwoo Lee https://orcid.org/0000-0002-5865-7924
Haimin Wang https://orcid.org/0000-0002-5233-565X

References

Brown, J. C. 1971, SoPh, 18, 489
Bučík, R. 2020, SSRv, 216, 24
Bučík, R., Innes, D. E., Guo, L., Mason, G. M., & Wiedenbeck, M. E. 2015, ApJ, 812, 53
Chen, B., Battaglia, M., Krucker, S., Reeves, K. K., & Glesener, L. 2021, ApJL, 908, L55
Chen, B., Gary, D., Yu, S., et al. 2023, BAAS, 55, 060
Chen, B., Kong, X., Yu, S., et al. 2024, ApJ, 971, 85
Chen, B., Shen, C., Gary, D. E., et al. 2020a, NatAs, 4, 1140
Chen, B., Yu, S., Reeves, K. K., & Gary, D. E. 2020b, ApJL, 895, L50
Costa, J. E. R., & Rosal, A. C. 2005, A&A, 436, 347
Dresing, N., Warmuth, A., Effenberger, F., et al. 2021, A&A, 654, A92
Dulk, G. A. 1985, ARA&A, 23, 169
Fleishman, G. D., & Kuznetsov, A. A. 2010, ApJ, 721, 1127
Garcia, H. A. 1994, SoPh, 154, 275
Gary, D., Chen, B., White, S., et al. 2023, BAAS, 55, 123
Gary, D. E., Chen, B., Dennis, B. R., et al. 2018, ApJ, 863, 83
Gieseler, J., Dresing, N., Palmroos, C., et al. 2023, FrASS, 9, 384
Gou, T., Liu, R., Su, Y., et al. 2024, SoPh, 299, 99
James, T., Subramanian, P., & Kontar, E. P. 2017, MNRAS, 471, 89
Kontar, E. P., Bian, N. H., Emslie, A. G., & Vilmer, N. 2014, ApJ, 780, 176
Kontar, E. P., & Reid, H. A. S. 2009, ApJL, 695, L140
Krucker, S., Hurford, G. J., Grimm, O., et al. 2020, A&A, 642, A15
Krucker, S., Kontar, E. P., Christe, S., Glesener, L., & Lin, R. P. 2011, ApJ, 742, 82
Krucker, S., Kontar, E. P., Christe, S., & Lin, R. P. 2007, ApJL, 663, L109
Lario, D., Balmaceda, L. A., Gómez-Herrero, R., et al. 2024, ApJ, 975, 84
Lemen, J. R., Title, A. M., Akin, D. J., et al. 2012, SoPh, 275, 17
Lin, R. P. 1974, SSRv, 16, 189
Lin, R. P. 1985, SoPh, 100, 537
Lin, R. P., Anderson, K. A., Ashford, S., et al. 1995, SSRv, 71, 125
Lin, R. P., Larson, D., McFadden, J., et al. 1996, GeoRL, 23, 1211
McMullin, J. P., Waters, B., Schiebel, D., Young, W., & Golap, K. 2007, ASPC, 376, 127
Mikić, Z., Linker, J. A., Schnack, D. D., Lionello, R., & Tarditi, A. 1999, PhPl, 6, 2217
Mondal, S., Battaglia, A. F., Chen, B., & Yu, S. 2024, ApJ, 966, 208
Moore, R. L., Cirtain, J. W., Sterling, A. C., & Falconer, D. A. 2010, ApJ, 720, 757
Müller, D., St. Cyr, O. C., Zouganelis, I., et al. 2020, A&A, 642, A1
Müller-Mellin, R., Böttcher, S., Falenski, J., et al. 2008, SSRv, 136, 363
Musset, S., Kontar, E. P., & Vilmer, N. 2018, A&A, 610, A6
Newkirk, G., Jr. 1967, ARA&A, 5, 213
Nita, G. M., Fleishman, G. D., Kuznetsov, A. A., et al. 2023, ApJS, 267, 6
Nitta, N. V., Bučík, R., Mason, G. M., et al. 2023, FrASS, 10, 50
Nitta, N. V., Mason, G. M., Wang, L., Cohen, C. M. S., & Wiedenbeck, M. E. 2015, ApJ, 806, 235
Nitta, N. V., Mason, G. M., Wiedenbeck, M. E., et al. 2008, ApJL, 675, L125
Nitta, N. V., Reames, D. V., De Rosa, M. L., et al. 2006, ApJ, 650, 438
Pesnell, W. D., Thompson, B. J., & Chamberlin, P. C. 2012, SoPh, 275, 3
Reames, D. V. 1999, SSRv, 90, 413
Reames, D. V. 2021, Lecture Notes in Physics, Vol. 978, Solar Energetic Particles. A Modern Primer on Understanding Sources, Acceleration and Propagation (Springer)
Richardson, I. G., von Rosenvinge, T. T., Cane, H. V., et al. 2014, SoPh, 289, 3059
Rodríguez-García, L., Gómez-Herrero, R., Dresing, N., et al. 2023, A&A, 670, A51
Rodríguez-Pacheco, J., Wimmer-Schweingruber, R. F., Mason, G. M., et al. 2020, A&A, 642, A7
Scherrer, P. H., Schou, J., Bush, R. I., et al. 2012, SoPh, 275, 207
Schwartz, R. A., Csillaghy, A., Tolbert, A. K., et al. 2002, SoPh, 210, 165
Shibata, K., Ishido, Y., Acton, L. W., et al. 1992, PASJ, 44, L173
Shibata, K., Masuda, S., Shimojo, M., et al. 1995, ApJL, 451, L83
Shibata, K., Shimojo, M., Yokoyama, T., & Ohyama, M. 1996, ASPC, 111, 29
Sterling, A. C., Moore, R. L., Falconer, D. A., & Adams, M. 2015, Natur, 523, 437
Stiefel, M. Z., Battaglia, A. F., Barczynski, K., et al. 2023, A&A, 670, A89
Strauss, R. D., Dresing, N., Kollhoff, A., & Brüdern, M. 2020, ApJ, 897, 24
Strauss, R. D., & Fichtner, H. 2015, ApJ, 801, 29
Strauss, R. D. T., Dresing, N., & Engelbrecht, N. E. 2017, ApJ, 837, 43
Stupishin, A. 2020, Magnetic-Field Library: NLFFF and Magnetic Lines, v3.4.23.1203, Zenodo, doi:10.5281/zenodo.3896222
Wang, L., Lin, R. P., Krucker, S., & Mason, G. M. 2012, ApJ, 759, 69
Wang, M., Chen, B., Knuth, T., et al. 2025, ApJ, 983, 33
Wang, M., Chen, B., Yu, S., et al. 2023, ApJ, 954, 32
Wang, W., Wang, L., Krucker, S., & Wimmer-Schweingruber, R. F. 2023, ApJ, 948, 51
Wang, W., Wang, L., Krucker, S., et al. 2021, ApJ, 913, 89
Wang, W., Wang, L., Li, W., et al. 2024, ApJ, 969, 164
Wang, Y. M., Pick, M., & Mason, G. M. 2006, ApJ, 639, 495
Warmuth, A., Schuller, F., Gómez-Herrero, R., et al. 2025, A&A, 701, A20
White, S. M., Benz, A. O., Christe, S., et al. 2011, SSRv, 159, 225
Wiedenbeck, M. E., Mason, G. M., Cohen, C. M. S., et al. 2013, ApJ, 762, 54
Xie, H., St. Cyr, O. C., Mäkelä, P., & Gopalswamy, N. 2019, JGRA, 124, 6384
Yu, S., Chen, B., Reeves, K. K., et al. 2020, ApJ, 900, 17